High-Resolution Soil-Moisture Maps Over Landslide Regions in Northern California Grassland Derived From SAR Backscattering Coefficients

Tien-Hao Liao, Seung-Bum Kim, Alexander L. Handwerger, Eric J. Fielding, Michael H. Cosh, *Senior Member, IEEE*, and William H. Schulz

***Abstract*—Slow-moving landslides are destabilized by accumulated precipitation and consequent soil moisture. Yet, the continuous high-resolution soil-moisture measurements needed to aid the understanding of landslide processes are generally absent in steep terrain. Here, we produce soil-moisture time-series maps for a seasonally active grassland landslide in the northern California coast ranges, USA, using backscattering coefficients from NASA's uninhabited aerial vehicle synthetic aperture radar at 6-m resolution. A physically based radar scattering model is used to retrieve the near-surface (5-cm depth) soil moisture for the landslide. Both forward modeling (backscattering estimation) and the retrieval (soil-moisture validation) show good agreement. The root-mean-square errors (RMSE) for vertical transmit vertical receive (*VV*) and horizontal transmit horizontal receive (*HH*) polarizations in forward model comparison are 1.93 dB and 1.88 dB, respectively. The soil-moisture retrieval shows unbiased RMSE of 0.054 m^3/m^3. Our successful retrieval benefits from the surface and double-bounce scattering, which is common in grasslands. The retrieved maps show saturated wetness conditions within the active landslide boundaries. We also performed sensitivity tests for incidence angle and found that the retrieval is weakly dependent on the angle, especially while using copolarized *HH* and *VV* together. Using the two copolarized inputs, the retrieval is also not sensitive to the change of orientation angles of grass cylinders. The physical model inversion presented here can be generally applied for soil-moisture retrieval in areas with the same vegetation cover types in California.**

***Index Terms*—Landslides, radar remote sensing, soil moisture.**

Manuscript received November 24, 2020; revised January 25, 2021; accepted March 9, 2021. Date of publication March 25, 2021; date of current version May 14, 2021. This work was supported in part by National Aeronautics and Space Administration under Contract 80NM0018D0004, which was carried out at the Jet Propulsion Laboratory, California Institute of Technology, and in part by Earth Surface and Interior Focus Area. *(Corresponding author: Tien-Hao Liao.)*

Tien-Hao Liao is with the Division of Geological and Planetary Sciences, California Institute of Technology, Pasadena, CA 91125 USA (e-mail: thaoliao@outlook.com).

Seung-Bum Kim is with the Jet Propulsion Laboratory, California Institute of Technology, Pasadena CA 91125 USA (e-mail: seungbum.kim@jpl.nasa.gov).

Alexander L. Handwerger is with the Joint Institute for Regional Earth System Science and Engineering, University of California Los Angeles, Los Angeles CA 91125 USA and also with the Jet Propulsion Laboratory, California Institute of Technology, Pasadena, CA 91109 USA (e-mail: alexander.handwerger@jpl.nasa.gov).

Eric J. Fielding is with the Jet Propulsion Laboratory, California Institute of Technology, Pasadena, CA 91125 USA (e-mail: eric.j.fielding@jpl.nasa.gov).

Michael H. Cosh is with the Hydrology and Remote Sensing Laboratory, USDA Agricultural Research Service, Beltsville, MD 20705 USA (e-mail: michael.cosh@usda.gov).

William H. Schulz is with the Landslide Hazards Program, United States Geological Survey, Denver, CO 80225 USA (e-mail: wschulz@usgs.gov).

Digital Object Identifier 10.1109/JSTARS.2021.3069010

I. Introduction

LANDSLIDES are costly and destructive natural hazards [1], [2] that commonly occur under wet conditions when soil moisture and pore-water pressures are high [3]–[5]. Climate change, which is altering both the frequency and magnitude of precipitation worldwide, is, thus, predicted to have a major impact on landslides [6]. Yet, the response of landslides to future climate change is difficult to assess due to uncertainties in both climate and landslide models. Constraining the soil-moisture conditions of active landslides will help to reduce the uncertainty in the climate and weather forcings that modulate landslide motion.

Persistently active slow-moving landslides provide an exceptional opportunity to investigate how the soil moisture impacts landslides. Slow-moving landslides, which move millimeters to meters per year [7], are destabilized by precipitation and can be monitored for decades using both remote-sensing- and ground-based techniques [8]–[11]. Ground-based instruments, such as soil-moisture sensors, piezometers, extensometers, and GPS, provide nearly continuous measurements of landslide hydrologic conditions, kinematics, and stress at specific locations within a landslide [11]–[13]. Broader views of landslides, which are necessary to fully capture the complex hydrology and kinematics of individual landslides and to simultaneously monitor hundreds of landslides over the entire mountain ranges, are provided by remote-sensing data that can be used to estimate soil moisture [14] and measure landslide displacements [8], [9], [15], [16]. Importantly, combined ground-based and remote-sensing-based investigations are needed to gain a complete picture of complex geophysical phenomena, such as landslides.

To investigate the relationship between the soil moisture and landslides requires the high-resolution spatial and temporal measurements of near-surface soil moisture in the landslide-prone regions. Merlin *et al*. [17] applied the disaggregation algorithm on data from the soil moisture and ocean salinity and moderate resolution imaging spectroradiometer (MODIS) to derive soil-moisture maps at 1-km spatial resolution. Paloscia *et al*. [18] applied machine learning techniques on data from the Copernicus Sentinel-1 synthetic aperture radar (SAR) scatterometer to construct soil-moisture maps at 1-km resolution. Foucras *et al*. [19] combined Sentinel-1 SAR, Sentinel-2 optical, and MODIS data to estimate soil moisture at a spatial resolution of 500 m

based on a change detection method. However, higher resolution data (tens of meters or better) can improve the understanding of how changes in soil-moisture impact relatively small features, such as landslides, which are often only a few tens of meters long and wide (although they can be much larger). Soil moisture may vary across small areas due to the changing slope inclination and aspect, material properties, and moisture recharge and drainage conditions.

Here, we use airborne SAR data to retrieve 6-m resolution maps of near-surface soil moisture (water volume/unit soil volume) over an active landslide site of 50 m by 300 m in the northern California coast ranges between 2017 and 2020. The data from the uninhabited aerial vehicle synthetic aperture radar (UAVSAR) are chosen because of its spatial resolution (1.7 m in the range direction for single look) and *L*-band ($\sim$23 cm) radar wavelength that is well suited for soil-moisture retrieval because it can penetrate through some (but not all) surface vegetation. We apply a single-scattering model to compute the copolarized backscattering coefficients of the grassland, which is the dominant land cover at our field site. The backscattering coefficient determines the proportion of incident wave energy, which is scattered from the grassland back in the direction of the incident wave. The single-scattering approach has been used for *L*-band for many vegetation types [20]–[25]. Several previous studies have developed alternative models for a variety of vegetated surfaces that can be used to infer soil moisture from the radar backscattering [26], [27]. In comparison, the single-scattering approach is faster to run and allows coherent simulation.

Our retrieval approaches are particularly suitable for landslide applications due to three factors as follows.

1) The physically based model is capable of rigorously simulating the backscattering across variable SAR incidence angles, which is important for SAR data in mountainous terrain.
2) The time-series retrieval [14], [28] explicitly estimates the unknown surface roughness at the microwave scale. While previous studies assumed the time-invariant roughness [29], [30], the surface roughness of the landslide is expected to change in time. Therefore, an explicit retrieval of the roughness is beneficial for the accurate soil-moisture estimates in landslide-prone terrain.
3) The generalized model from this study can be applied to grass-covered landscapes, in general.

Our work is novel for the following reasons.

1) We develop an approach that uses backscattering coefficients to derive soil-moisture maps from UAVSAR that allows us to capture the complex near-surface hydrology. Furthermore, our approach can be applied to simultaneously monitor hundreds of landslides over the entire mountain ranges.
2) The derived soil-moisture maps provide the high-resolution (6-m) measurements.
3) We use a physical model that makes it possible to apply the same retrieval algorithm to other landslide sites with a similar vegetation cover.

The goal of this article is to present a framework to generate high-resolution soil-moisture maps that can be used to analyze relationships between the landslide activity and wetness conditions. The rest of this article is organized as follows. Section II describes the study area; Section III describes the methodology including the physically-based model, time-series retrieval, and antecedent precipitation Index- [(API); (8)] based soil-moisture estimation; Section IV describes the results and discussions; and finally, Section V concludes the article.

II. Study Area

Our study is focused on the Two Towers landslide located in the Eel River catchment, northern California coast ranges [11]. The U.S. Geological Survey established a long-term monitoring station on the landslide in 2014, which includes hourly measurements of rainfall and soil moisture [31], [32]. Soil moisture and rainfall were measured from January 1, 2017, through April 29, 2020, with soil moisture measured at a depth of 19 cm below the ground surface [32]. The region has a Mediterranean climate, characterized by a cool wet season and a warm dry season. Mean annual rainfall was $\sim$1.6 m/yr at the Two Towers monitoring location for the 2016 through 2020 water years, most of which fell between October and May. A water year is a term in hydrology to describe a time period of 12 months for which precipitation total is measured. For our study area, the water year begins October 1 and ends September 30. The mean annual temperature for the 2016 and 2020 water years was $\sim$13.8 °C with a maximum temperature of $\sim$31.9 °C and a minimum of $-$1.3 °C [33].

Fig. 1 shows the location of the Two Towers landslide and several additional soil-moisture monitoring sites in northern California that are managed by the National Oceanic and Atmospheric Administration (NOAA). The *in situ* sites are used to help constrain the estimation of 5-cm-depth soil moisture at Two Towers. Table I lists the landcover and information for marked sites in Fig. 1(a). Their soil texture, vegetation cover, and environmental conditions, including rainfall patterns, temperature, and geology, are similar to those at Two Towers.

Fig. 1(a) also shows the UAVSAR coverage for track 24 500, which was used for soil-moisture retrieval over the study area.[1] Fig. 1(b) shows a close look at the Two Towers landslide with the black lines highlighting the active landslide area. The water content sensor is shown by the red dot and the rain gauge is located a few meters north.

The Two Towers landslide is $\sim$250 m long, has an average width of $\sim$40 m, the thickness of 7 m, and a slope angle of $\sim$15° (see Section IV-B) [11]. The downslope motion of Two Towers, and hundreds of other nearby slow-moving landslides [9], is modulated by seasonal rainfall that acts to increase the soil moisture and pore-water pressure, which in turn reduces the effective normal stress and shear strength [5]. The motion of the Two Towers landslide was found to be strongly controlled also by variable soil swell pressure, which partly counteracts seasonal reductions in shear strength [11]. The total seasonal displacement of Two Towers varies each year and depends on the amount of rainfall [11]. For instance, during the dry 2015 and average 2016 water years, the landslide moved $\sim$6 mm

[1] Online. [Available]: https://uavsar.jpl.nasa.gov/

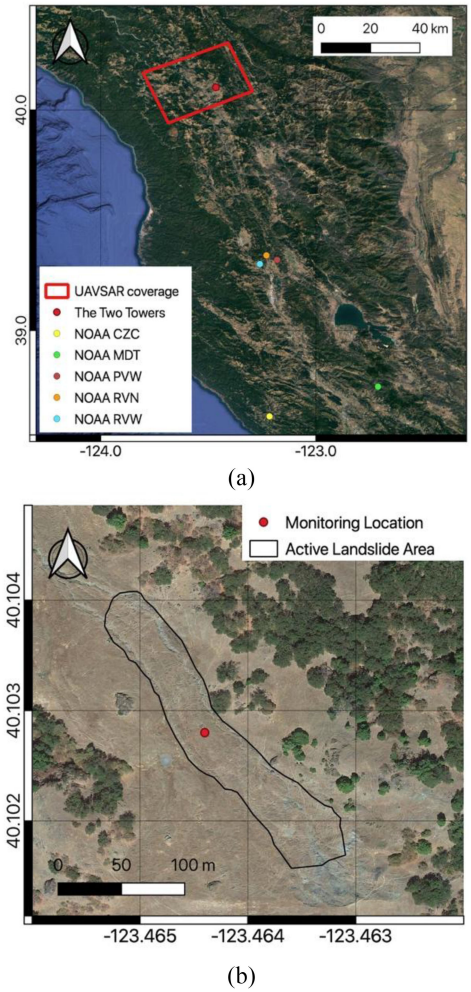

Fig. 1. Google Earth imagery for the northern California coast range field site. (a) Overview map showing the location of soil-moisture monitoring sites used in this study. The UAVSAR coverage from the track 24 500 is shown by the red box. (b) Two Towers landslide boundaries are shown by the black line and the red circle shows the soil-moisture monitoring site [34].

and ∼20 mm, respectively. With a large increase in rainfall in the 2017 water year, one of the wettest years on record in California, the landslide moved 44 mm. A similar relative change in the seasonal displacement with rainfall has been observed for dozens of nearby landslides [9]. The landslide movement in Fig. 1(b) is to the northwest.

The Two Towers landslide occurs within the central belt of the Franciscan mélange, which is a lithologic unit with an argillaceous matrix surrounding the blocks of more competent rocks, including sandstone, greenstone, and chert [37], [38]. The Two Towers landslide material contains clay minerals, such as chlorite, illite/mica, and smectite [11]. Recent work by Hahm *et al*. [39] characterized the critical zone (i.e., the distance from the ground surface to the unweathered bedrock) at one location within the central belt of the Franciscan mélange. They found that this lithologic unit at their site has a thin critical zone that is <4 m thick and thin soil cover (<1 m). The critical zone in the mélange also has low hydraulic conductivity with values between 10^{-6} and 10^{-8} m/s [40]–[42]. The combined effect of the

TABLE I
REFERENCE SOIL-MOISTURE SITES

In situ location	Landcover *	Clay fraction	5 cm depth soil moisture (m^3/m^3)
NOAA-Redwood Valley – North (RVN)	Shrubland	0.228	0.047~0.42
NOAA-Potter Valley – West (PVW)	Shrubland	0.21	0.07~0.495
NOAA-Redwood Valley – West (RVW)	Shrubland	0.203	0.041~0.624
NOAA-Middletown (MDT)	Shrubland	0.169	0.048~0.366
NOAA-Cazadero (CZC)	Grassland	0.265	0.101~0.429
Two Towers	Grassland	0.22	Estimated by API

*Landcover from National Land Cover Database 2016 [35] for NOAA sites. Landcover of the Two Towers is from *in situ* observation. Clay fraction is from the soil survey geographic database [36]. The landcover at Two Towers is from field investigation. The maximum and minimum soil moisture (Mv) at 5-cm depth are reported for the training period over 3 years from 2016 to 2018.

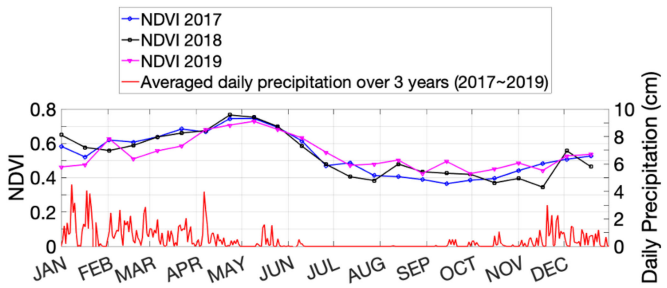

Fig. 2. Seasonal vaiation over the Two Towers landslide location using NDVI from MODIS from 2017 to 2019. Field photographs from 2012 to 2018 (W. Schulz, public domain) are provided in the appendix.

thin critical zone, low hydraulic conductivity, and high seasonal rainfall acts to keep the groundwater table near the ground surface year round and often leads to fully saturated hillslopes during the wet season [11], [41], [42]. Hahm *et al*. [39] found that only ∼200 mm of rainfall is needed to reach full hillslope saturation at their study site. Other than the saturation situation, other studies have shown a rapid rise in groundwater shortly after the onset of seasonal precipitation [11], [41].

The region underlain by the central belt of the Franciscan mélange is classified as a sparse deciduous oak, annual grass, savanna-woodland [39]. Field investigation of the Two Towers landslide shows that the vegetation on the landslide surface is mostly annual grasses (see Fig. 2). While a detailed study of the vegetation cover has not been performed at Two Towers,

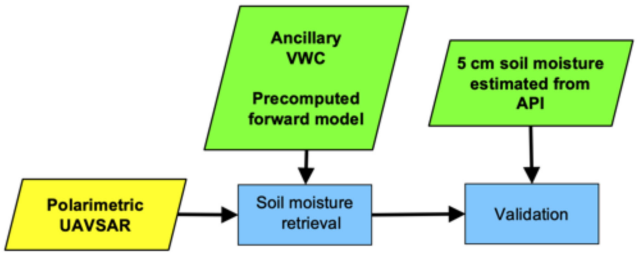

Fig. 3. Algorithm flowchart for time-series retrieval of soil moisture and the validation.

Hahm *et al*. [39] for the same region documented slender oat (*A. barbata*), foxtail barley (*H. murinum*), filaree (*E. cicutarium*), medusahead (*T. caput-medusae*), velvet grass (*H. lanatus*), and Italian thistle (*C. pycnocephalus*). Hahm *et al*. [39] suggest that annual grasses cover this landscape because they can survive the dry-season conditions and essentially flooded wet-season conditions.

The seasonal precipitation of the northern California coast ranges is reflected in the vegetation greenness by analyzing the normalized difference vegetation index (NDVI). NDVI is derived from the difference vegetation index (DVI) to characterize vegetation trends in coverage. NDVI is derived from atmospherically corrected reflectance in the red and near-infrared wavebands [43]. Fig. 2 shows the NDVI time series from MODIS for an area of the landslide from 2017 to 2019 [44]. By plotting the data into a single-year time frame, we observe similar seasonal trends. NDVI is at its maximum in May, meaning the grass is greener with higher moisture content, and at its minimum in July, meaning the grass is at its driest. In Appendix B, several *in situ* photos taken between 2012 and 2018 show the greenness of grass at different times of the year. The grass is dry and brown between June and September, which correlates to low NDVI. The average annual daily precipitation over 3 years, from 2017 to 2019, is plotted alongside NDVI. A higher NDVI follows the rainy season.

III. Methodology

In this section, we describe our methods for soil-moisture retrieval from polarimetric UAVSAR data. These data were acquired on flight path ID 24 500 with 8 flights between March 2017 and February 2020 (2017.3.7, 2017.10.30, 2018.2.9, 2018.7.23, 2018.10.9, 2019.2.21, 2019.5.30, and 2020.2.27). UAVSAR has a high spatial resolution with a pixel spacing of 1.67 m in the range direction and 0.6 m in the azimuth direction. We multilook the data to a ∼6-m pixel spacing by taking 3 looks in the range and 12 looks in the azimuth. This reduces the radar speckle noise from 3 to 0.67 dB. UAVSARs calibration error is 0.3 dB and the root-mean-square error (RMSE) is 0.73 dB. Considering the dynamic range of bare soil is 5–10 dB [28] or smaller when attenuated by vegetation, the 6-m pixel resolution has sufficient radiometric accuracy for soil-moisture retrieval.

Fig. 3 shows the soil-moisture retrieval flowchart. Each step in the flowchart will be described in detail. We start by describing the soil-moisture time-series retrieval. Next, we describe the forward model used to generate the lookup tables (LUTs). To facilitate the fast and accurate inversion of soil moisture, the outputs of the physical model are provided as LUTs (with three axes) for a single incidence angle. The three axes are the real part of the dielectric constant of soil, soil surface root-mean-square (RMS) height, and vegetation water content (VWC). For the forward model, VWC is needed to estimate the geometry parameter. We use an NDVI-based estimation of VWC for the study area. Finally, we use an accumulative precipitation-based method to compute soil moisture for the validation of the retrieval algorithm.

A. Soil-Moisture Time-Series Retrieval

A time-series retrieval of soil moisture for N_t time points is performed by minimizing a cost function defined as [14], [46]

$$\text{cost} = \sum_{n=1}^{N_t} \Big[\left(\sigma_{VV}^{\text{LUT}} \left(h, \varepsilon_n, \text{VWC}_n \right) - \sigma_{VV,n}^{\text{mea}} \right)^2 + \left(\sigma_{HH}^{\text{LUT}} \left(h, \varepsilon_n, \text{VWC}_n \right) - \sigma_{HH,n}^{\text{mea}} \right)^2 \Big]. \quad (1)$$

The LUT contains the precomputed backscattering (in decibel), σ_{VV}^0 and σ_{HH}^0 based on the three parameters, roughness height (h), soil dielectric constant (ε_r), and VWC. *VV* and *HH* refer to the polarized UAVSAR data and stand for vertical transmit vertical receive and horizontal transmit horizontal receive, respectively. The forward model is precomputed for a full range of soil moisture, surface roughness, and VWC, and fills 3-D LUTs for *HH* and *VV*. The minimum cost functions are searched within LUTs during the soil-moisture retrieval. The measured backscattering data are shown with the superscript, mea. Without losing the generality, the roughness is assumed to be the same over time that reduces to a single h value to be retrieved. The total unknowns for the retrieval become $2N_t + 1$, $2N_t$ from N_t soil dielectric constants, and N_t VWCs. However, there are only $2N_t$ backscattering measurements from the UAVSAR data and the cost function is underdetermined. To make (1) well determined, we apply VWC estimated from NDVI as a known parameter to reduce the total unknowns to $N_t + 1$. Given the same $2N_t$ observables, (1) is now well conditioned to calculate a soil-moisture time series that best fits the LUT. Although we assume time-invariant roughness during our relatively short study period [29], [30], which is appropriate for slow-moving landslides, an explicit retrieval of the time-dependent roughness may be beneficial for the accurate soil-moisture estimates in landslide-prone terrain. In particular, the surface roughness of faster moving landslides will change over shorter time periods such that the measurements of surface roughness change before and after the landslide motion would lead to improved estimates of soil moisture.

A progressive retrieval consisting of two steps is performed by varying VWC at each time point within 10% of the NDVI-VWC to minimize the cost function. The purpose is to seek better retrieval at the second step using the results of the first step as a first guess.

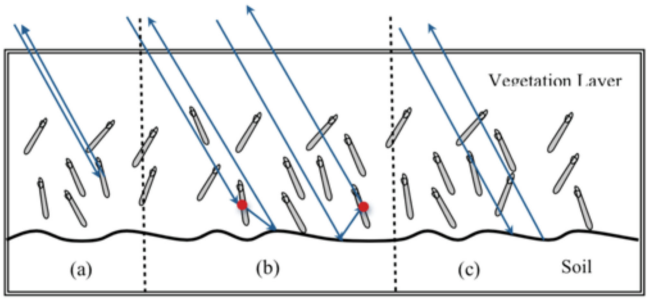

Fig. 4. Schematic cartoon showing expected SAR scattering in a grassland from the distorted born approximation. (a) Volume scattering. (b) Double-bounce scattering. (c) Surface scattering.

B. Radar Scattering Model for Grassland

Here, we outline our physically based model for radar backscattering. To save computational time, an LUT representation of the forward model is used during the retrieval. A single-scattering model known as the distorted born approximation is applied to simulate backscattering from a grassland [20], [22], [27]. The model is constructed by three scattering mechanisms: volume scattering, double-bounce scattering, and surface scattering.

Fig. 4 shows a schematic perspective cartoon of scattering from discrete objects with shapes that can approximate grassland (i.e., cylinders). In our model for grasslands, we only use cylinders to simulate the stems of the grass. Equations (2)–(4) are for copolarized backscattering from three scattering mechanisms: volume scattering, double-bounce scattering, and surface scattering, respectively

$$\sigma_{\beta\beta}^{\mathrm{vol}} = 4\pi \frac{N_A}{d} \frac{1 - e^{-4dIm(k_{\beta z})}}{4Im\left(k_{\beta z}\right)} \langle |f_{\beta\beta}\left(\theta_i, \pi; \pi - \theta_i, 0\right)|^2 \rangle \tag{2}$$

$$\sigma_{\beta\beta}^{DB} = 16\pi N_A r_\beta e^{-4Im(k_{\beta z})d} \langle |f_{\beta\beta}\left(\pi - \theta_i, \pi; \pi - \theta_i, 0\right)|^2 \rangle \tag{3}$$

$$\sigma_{\beta\beta}^{\mathrm{Surf}} = e^{-4Im(k_{\beta z})d}\, \sigma_{\beta\beta}^{(\mathrm{bare\ soil})} \tag{4}$$

where β stands for vertical (V) or horizontal (H) polarization, N_A is the area density of the cylindrical scatterers (m^{-2}), d is the vegetation layer depth (m), k_z is the vertical wavenumber, r is the reflectivity, and $\sigma^{(\mathrm{bare\ soil})}$ is the backscattering from bare soil. In our model, the bare soil backscattering is from the precomputed LUT using numerical Maxwell's equation 3-D (NMM3D) [45]. $f(\theta_s, \phi_s; \theta_i,\ \phi_i = 0)$ is the scattering amplitude of the cylinder with incident angle $(\theta_i,\ \phi_i = 0)$ and scattering angle (θ_s, ϕ_s). θ is the elevation angle referenced to the normal of the surface, and ϕ is the azimuth angle referenced to the projected incident wave's direction on the surface. The $\langle\rangle$ is for the ensemble average over cylinders, either sizes or the orientation, with the incident angle θ_i. The above-mentioned parameters all have two representations for *VV* and *HH* polarizations. The overall backscattering is the incoherent summation of the three scattering mechanisms from (2) to (4). The extinction coefficients result in the attenuation in the term $2Im(k_{\beta z})$. The factor of 4 in double bounce and surface accounts for the round trip of the radar waves. The dielectric constant inside the vegetation layer is considered by the effective dielectric constant, which comes from the extinction coefficients of the vegetation [26].

The distinction between the physically based model and semiempirical (or machine learning) approaches [18] is that the physically based model has the potential to apply to grass vegetation generally in different locations and time periods. The model requires information on the vegetation structure, VWC, and radar scattering coefficient [14].

We use cylinders to model the grass on the landslide surface that is defined by radius (a), length (l), moisture content ($M\mathrm{veg}_{\mathrm{pasture}}$), and orientation. VWC varies with time and is controlled by the density N_A (kg/m^2). Orientation angles are uniformly distributed between 0° and 66°.

$$N_A = \frac{\mathrm{VWC}}{\rho_{\mathrm{water}} \pi a^2 l M\mathrm{veg}_{\mathrm{pasture}}}. \tag{5}$$

Besides the vegetation parameters, soil roughness is also required for the radar scattering model. We used 1 cm for RMS height representing soil roughness, which was measured in the field during July 2020. Correlation length measurement is known to have large uncertainty (50% uncertainty) [46]. Consequently, we treated the ratio of correlation length to RMS height as a fitting parameter, and the ratio is set to 4.

C. VWC Estimation From NDVI

We convert NDVI to VWC using empirical relationships [47]–[49]. However, there are significant differences in the dynamic range of VWC based on NDVI for grasslands. To determine how the estimated VWC varies as a function of NDVI, we examined NDVI from medium- to high-resolution satellite imagery, including Landsat (30-m pixel) and Planet Labs imagery (3-m pixel) [50], [51]. There is good agreement between the NDVI measured from Landsat and Planet Labs in Section IV-B, indicating it as appropriate to use data from either instrument. Due to the longer time record and open access to the data, we selected Landsat NDVI for our time-series analyses.

Next, we compared the measured with estimated VWC. We measured the *in situ* VWC in the field on July 24, 2020. *In situ* VWC was measured at 0.18 kg/m^2 using an oven drying technique for an area of 1 m^2. We then estimated VWC from NDVI using Allahmoradi's formula [47], which is defined as

$$\mathrm{VWC} = 1.93\mathrm{NDVI}^2 - 0.21\mathrm{NDVI} + 0.01. \tag{6}$$

The NDVI on 2020.7.24 was 0.41 from Planet Labs data, which results in a VWC of 0.25 kg/m^2, slightly higher than the *in situ* value. The seasonal range of NDVI is about 0.4 to 0.8 (see Fig. 2), which results in a VWC range from 0.24 to 1.08 kg/m^2.

D. Soil-Moisture Estimation From Antecedent Precipitation Index (API)

The measurements of near-surface soil moisture are essential for model validation. The forward model and the retrieval mentioned above are developed for the near-surface soil moisture with depths of 0–5 cm. However, at the landslide location, we

do not have the *in situ* measurement of soil moisture within the top 5 cm. The soil-moisture data closest to the surface at Two Towers are from 19 cm depth.

To help constrain the near-surface soil moisture at Two Towers, we use a daily diagnostic soil-moisture equation [52], [53]. The daily diagnostic soil-moisture equation is defined as

$$M_v = M_{v,re} + (M_{v,e} - M_{v,re})\left(1 - e^{-c_4 B}\right) \quad (7)$$

where M_v, $M_{v,e}$, and $M_{v,re}$ are the soil moisture, saturation, and the residual soil moisture, respectively. The soil moisture depends on the antecedent precipitation index (API), B, which is a fit exponent, and is bounded between $M_{v,e}$ and $M_{v,re}$ with an exponential variation. c_4 is one of four coefficients needed to be determined from the training data. B is defined as

$$B = \sum_{i=2}^{n-1}\left[\frac{P_i}{\eta_i}\left(1 - e^{-\frac{\eta_i}{z}}\right) e^{-\sum_{j=1}^{i-1}\frac{\eta_j}{z}}\right] + \frac{P_1}{\eta_1}\left(1 - e^{-\frac{\eta_1}{z}}\right) \quad (8)$$

where P_i is the daily precipitation i days prior to the observation date, z is the depth where the soil moisture is estimated, and η_i scales the contribution of the precipitation from i days before the observation. The η_i term accounts for the decay in soil moisture over time after a rainfall event is defined as

$$\eta_i = c_1 + c_2 \sin\left[\frac{2\pi\,(\mathrm{DOY}_i + c_3)}{365}\right]. \quad (9)$$

The coefficients in (7)–(9) are determined using a set of training data, soil moisture, and API. We used training data from five NOAA field locations in northern California that have continuous soil-moisture measurements at multiple depths over 3 years from 2016 to 2018 [see Fig. 1(a)]. We selected sites that share similar soil textures, lithology, and climate with the Two Towers landslide. After determining the best-fitting coefficients from these data, we estimated the Two Towers soil moisture at 5-cm depth. More details regarding the daily diagnostic soil-moisture equation are listed in the Appendix.

IV. Results and Discussion

In this section, we begin by describing our results for the validation of soil-moisture data. Then, we present the forward model and the retrieval results. The time-series maps of retrieved soil moisture are then shown for the active landslide area. Finally, we perform a sensitivity test of the retrieval performance.

A. *Estimation of 5-cm* in Situ *Soil Moisture*

As described above, we selected five NOAA field sites that record *in situ* soil moisture at 5-cm depth to calibrate the daily diagnostic soil-moisture equation over 3 years from 2016 to 2018. Using these data, we determined the c-coefficients in 7–9 (see Table II). We then grouped the observation data into training (2016.1.1–2018.12.31) and validation (2019.1.1–2020.4.29) sets. For the training data, we used c-coefficients to calculate the entire time series of soil moisture at 5-cm depth. For the validation data, we computed the RMSE and the correlation (r) between the estimated and *in situ* soil moisture for each individual site. We found the lowest RMSE and best correlation

TABLE II
Estimated c-Coefficients and the Validation of Estimated Soil Moisture at 5 cm Within Each NOAA Site (RMSE and CORR)

In situ location	(c_1, c_2, c_3, c_4)	RMSE* (m^3/m^3)	CORR*
NOAA-RVW	(0.2, 0.1, 31, 0.5)	0.045	0.92
NOAA-PVW	(0.3, 0.1, 241, 0.5)	0.058	0.93
NOAA-RVN	(0.3, 0.1, 211, 0.4)	0.07**	0.93
NOAA-CZC	(0.1, 0.1, 271, 0.2)	0.052	0.91
NOAA-MDT	(0.1, 0.1, 31, 0.2)	0.052	0.86

* Mv for soil moisture.
** Large RMSE is due to floods in winter (~0.7 m^3/m^3).

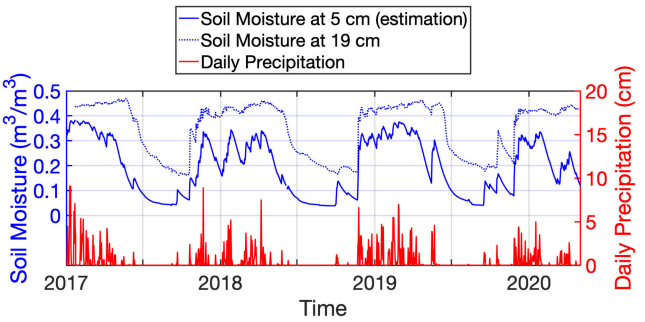

Fig. 5. Soil-moisture time series at the Two Towers landslide, northern California. Soil moisture at 19-cm depth is measured, and soil moisture at 5-cm depth is calculated using (7).

occurred at the RVW, PVW, and RVN sites (see Fig. 1 and Table II). However, we note an unusually high soil-moisture reading at the RVN site with values up to 0.7 m^3/m^3, which we interpret to be a flooded sensor. Thus, we selected the c-coefficients from RVW and PVW to apply to the Two Towers landslide.

Using (7) and the two sets of the c-coefficients from RVW and PVW, respectively, we calculated two sets of soil-moisture time series using the precipitation data measured at the Two Towers landslide and take the average of them to give the estimation of soil moisture at 5 cm for the Two Towers. The residual and saturated soil-moisture values were computed using the standard soil texture table, and they are 0.061 m^3/m^3 and 0.40 m^3/m^3, respectively. The residual soil-moisture value from the texture table agrees with the residual *in situ* 5-cm soil moisture we measured on July 24, 2020, which was 0.055 m^3/m^3. Fig. 5 shows the calculated 5-cm soil moisture, measured 19-cm soil moisture, and measured precipitation at the Two Towers landslide. The soil moisture measured at 19 cm was always greater than the calculated moisture at 5 cm and this phenomenon is also observed in the *in situ* measurement at RVW and PVW while comparing soil moisture at 20 cm to that at 5 cm.

B. *Remote-Sensing Data Over the Active Landslide Area*

Fig. 6 shows an overview of the focus area within the Two Towers landslide. Fig. 6(b) shows an example of *HH* backscattering from October 9, 2018. We apply a flat surface model and use the local incidence angle for the physically based model.

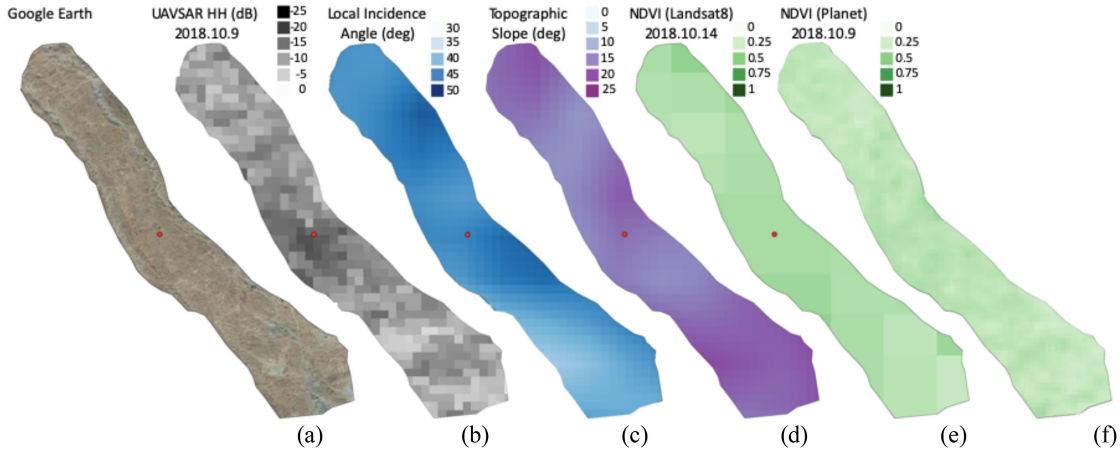

Fig. 6. Remote-sensing datasets used to investigate the active landslide area at Two Towers. (a) Google Earth optical image. (b) UAVSAR *HH* (σ^0) in dB from flight Eel River 24 500 acquired on 2018.10.9. (c) Local incidence angle from UAVSAR flight Eel River 24 500. (d) Topographic slope (in degrees) from SRTM. (e) NDVI from Landsat 8 acquired on 2018.10.14. (f) NDVI from Planet Labs acquired on 2020.7.24. Pixel sizes are as follows: 6×6 m for (b)–(d), 30×30 m for (e), and 3×3 m for (f).

The local incidence angle is the angle between the normal of the terrain and the looking vector of the UAVSAR. We calculated the terrain slope angle using a ∼30-m pixel spacing shuttle radar topography mission (SRTM) digital elevation model (DEM) [see Fig. 6(d)] and a 1 m lidar DEM provided by open topography [54]. The mean slope angle at the monitoring location (red dot) is approximately 15° and 10.4° using the SRTM and lidar DEM, respectively. The ∼5° difference in slope angle is due to the differences in the data resolution. We will discuss how errors in the slope data may impact the soil-moisture retrieval in Section IV-E. The local incident angle is about 44°. Within the active landslide area in Fig. 6, the angle varies from 30° to 50°. Since landslides occur over a large area (hundreds of meters), the retrieval algorithm needs to be robust across incidence angles, as verified in Section IV-E. Fig. 6(e) shows the NDVI from Landsat 8 on October 14, 2018. The monitoring location is located close to the center of four pixels [see the red dot in Fig. 6(b)]. We take an average of the four surrounding pixels to calculate the representative values for Two Towers.

C. Forward Model Verification

To test allometry equations for vegetation parameters, we compared values with the ground-based measurements from July 2020. We measured vegetation moisture content at two different sites, one with short grass and the other with tall grass. The vegetation moisture content, $M\mathrm{veg}_{\mathrm{pasture}}$, was 0.17 $\mathrm{m}^3/\mathrm{m}^3$ and 0.28 $\mathrm{m}^3/\mathrm{m}^3$ for the short and tall grass, respectively. The radius ranged from 0.68 to 1.22 mm with an average of 0.95 mm. The lengths for short and tall grass were 0.25 m and 0.6 m, respectively. The densities of short and tall grasses were 84 and 200 cylinders/m^2. The calculated VWCs by the allometry equations for the short and tall grass were 0.04 and 0.16 kg/m^2, which agree well with the oven-drying VWC values of 0.05 and 0.18 kg/m^2. The allometry equation is, thus, validated. However, because July 2020 measurements do not coincide with the UAVSAR flights in 2017–2019, we cannot validate the NDVI-derived VWC values concurrent with the UAVSAR flights. Therefore, we approximated the parameter sets of VWC using more extensive ground measurements of plant geometry from grasslands collected during the SMAPVEX12 field campaign in the summer of 2012 over rain-fed Canadian Prairies near Winnipeg [55]. SMAPVEX12 is the primary prelaunch field campaign for the soil-moisture active passive (SMAP) mission, established to provide data for algorithm evaluation and testing. From the field observation as well as field photos obtained at both SMAPVEX12 and Two Towers, we observe the similarity in terms of vegetation structures. We then used 2.1 mm, 30 cm, and 0.6 $\mathrm{m}^3/\mathrm{m}^3$ for the radius, length, and moisture content, respectively, to model the grass. As a result, there are 80 grass cylinders per square meter, for example, when VWC $= 0.2$ kg/m^2. The seasonal measurements of grass structures and density at the Two Towers landslide site would improve the understanding of variability that could impact modeling results.

Fig. 7 shows the comparisons of backscatter (*VV* and *HH*) measured from UAVSAR with values simulated by our forward model. We align the data in Fig. 7 based on the day of year (DoY) of the data acquisitions (thus, multiple years are overlaid within one year). We found that both *VV* and *HH* showed similar backscatter trends and that the modeled backscatter captures the seasonal trend of VWC at the Two Towers landslide.

To better understand the success of the forward model simulating the observation, we examine the detailed scattering mechanisms. Fig. 8 shows the scattering decomposition of *VV* and *HH*. For *VV*, volume and surface scattering are dominant. For *HH*, double-bounce scattering and volume scattering are dominant. Modeled *HH* shows better agreement with observations than *VV* does in both RMSE and the correlation.

The surface scattering contributes significantly even with VWC of ∼0.6 kg/m^2 (very large for grassland), using the correlation length to RMS height ratio equal to 4. Volume scattering and surface scattering are comparable for *VV*. Double-bounce scattering and volume scattering are comparable for *HH*. Both the dominant scattering mechanisms for *VV* and *HH* here have

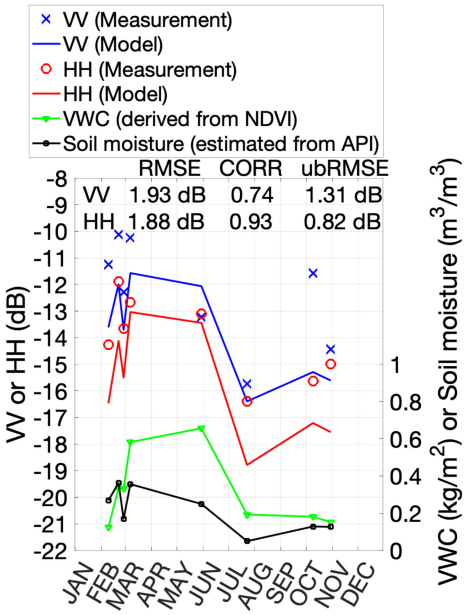

Fig. 7. Forward model comparison of *VV* and *HH* between UAVSAR measurement and the physical model. Soil moisture is at a 5-cm depth estimated from API. VWC is derived from NDVI.

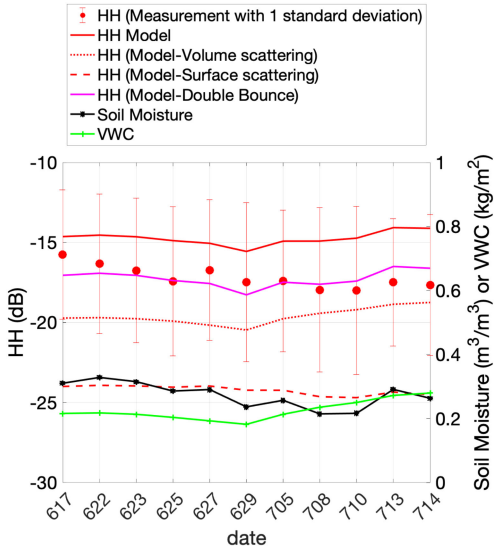

Fig. 9. Verification that the same physical model successfully applied to a different location of grassland landcover type by simulating the UAVSAR observations during the SMAPVEX12 campaigns. "617" and "714" refer to June 17 and July 14, respectively, for example.

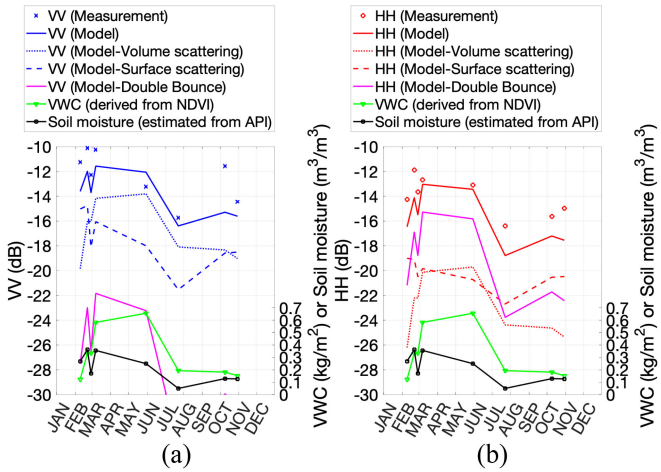

Figure 8. Scattering decomposition (volume scattering, double-bounce scattering, and surface scattering) for (a) *VV* and (b) *HH*.

soil-moisture dependence through either surface scattering or double-bounce scattering. The UAVSAR backscattering also has a significant correlation to soil moisture, 0.84 for *VV* and 0.92 for *HH*. Since both the model and measurement have dependence on soil moisture, the retrieval is expected to be sensitive enough to capture the soil-moisture change. Moreover, the UAVSARs data provide the full covariance matrix elements, so we also perform the Freeman–Durden decomposition for the entire time series. We find either surface scattering or double-bounce scattering dominating the decomposition in each date. Our findings indicate that the UAVSAR data are sensitive to soil moisture. Furthermore, our findings are consistent with the results, as shown in Fig. 8, except Fig. 8 shows more detail for the decomposition for the individual *VV* and *HH* polarizations.

The primary merit of a physical model is that the same model can be applied to the different regions of the same vegetation cover because the scattering physics are consistent. Grassland was previously modeled for validating simulation and retrieval for the SMAPVEX12 field campaign [55]. Fig. 9 shows that the same single-scattering model developed in this study accurately simulates the SMAPVEX12 UAVSAR observations. The differences between the Two Towers landslide and SMAPVEX12 are as follows: First, VWC changed seasonally from 0.2 to 0.7 kg/m^2 at Two Towers, while it stayed at ~0.2 kg/m^2 during one month in Winnipeg; second, grass stalk has vertical orientation at Two Towers (0°–55°) and uniform orientation in Winnipeg (0°–90°). In summary, the same scattering model is successfully adaptable to two distinctively different regions in simulating the UAVSAR observations.

D. Soil-Moisture Retrieval and Validation

Fig. 10 shows the time-series soil-moisture retrieval. Mironov's model is applied to convert between the soil moisture and the dielectric constant [56]. We performed the retrieval progressively in two steps. In the first step, we use the first-guess VWC derived from NDVI to search the LUTs of *VV* and *HH* to calculate the cost function, as described in (1). For the second step, we allow the individual VWC to vary within 10% from the first guess. Since VWC in the first guess is not from *in situ* but derived from NDVI, this 10% variation of VWC is considered as the dynamic range of VWC for the study area. Table III presents the performance of the first and second retrieval of soil moisture against the soil moisture estimated from API. We observed that the performance of our soil-moisture retrieval is

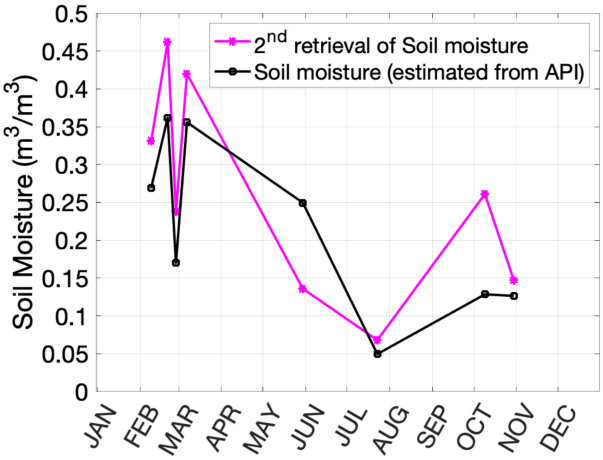

Fig. 10. Soil-moisture estimates after the second step of the progressive retrieval using *HH* and *VV*.

TABLE III
RMSE, CORRELATION, AND UBRMSE OF THE FIRST AND SECOND RETRIEVED SOIL MOISTURE AGAINST THE ESTIMATED SOIL MOISTURE FROM API

Polarization	RMSE (1^{st},2^{nd})	CORR (1^{st},2^{nd})	ubRMSE (1^{st},2^{nd})
HH&VV	0.068, 0.066	0.88, 0.89	0.058, 0.055
VV-only	0.113, 0.112	0.74, 0.73	0.109, 0.108
HH-only	0.055, 0.054	0.88, 0.88	0.055, 0.054

∗unit for RMSE and ubRMSE: (m^3/m^3).

slightly improved for the *HH*-only results. The improved RMSE and unbiased RMSE (ubRMSE) are both 0.054 m^3/m^3.

The time-series retrieval is then applied to the active landslide area, as shown in Fig. 1(b). Each pixel contains a time series of eight data values from the coregistered maps of *VV*, *HH*, and derived VWC from NDVI. The progressive retrieval is iterated for each pixel using *HH* and *VV* inputs to estimate the cost function. The retrieved near-surface soil-moisture maps are shown in Fig. 11 . The soil-moisture map of July 23, 2018, shows dry conditions along the landslide. The soil moisture begins to increase after the start of rainfall, which is in October each year (see Fig. 2). The wet-season soil-moisture maps between November and May show generally wet conditions throughout the landslide with some areas of higher moisture content toward the northern and southern extent of the landslide. These relatively wet areas do not coincide with the patterns of local incidence angle, topographical slope, or NDVI (see Fig. 5), which suggests the pattern is characterized by true soil-moisture changes. These patterns are more obvious when the overall soil-moisture content is higher in this area. The soil-moisture map of March 7, 2017, shows a more saturated pattern because the current LUT is only calculated up to the soil dielectric constant of 30 corresponding to ∼0.46 m^3/m^3 in this area, given the soil clay fraction of 0.22. By expanding the spatial domain of our analysis to include areas with active landslides and stable hillslopes, we may be able to identify perpetually wet hillslopes that may be more likely to fail as a landslide.

TABLE IV
FORWARD MODEL COMPARISON BY VARYING LOCAL INCIDENCE ANGLE (CONSIDERED AS THE UNCERTAINTY RESULTING FROM THE DEM)

Polarization	RMSE (dB)	CORR	ubRMSE (dB)
VV	1.14,1.93,2.35	0.84,0.74,0.71	1.14,1.31,1.35
HH	0.64,1.88,2.4	0.95,0.93,0.89	0.62,0.82,0.96

∗Statistics are for incidence angles at 30°, 40°, and 50°, respectively from left to right.

A previous study applied machine learning methods to retrieve soil moisture from SAR data in mountainous areas with a retrieval RMSE between 0.045 and 0.07 m^3/m^3 with 150 m resolution [57]. The comparable performance of our method with this previous work suggests that our physically based model can be applied to general conditions for grassland at various slope angles. Thus, our method is especially useful in areas where the training data have not been acquired for machine learning. The physical model inversion covers the full dynamic range of input variables of interest by extending the scattering physics.

The scientific measurement requirement from the NASA SMAP mission for soil moisture is 0.04 m^3/m^3 volumetric accuracy in the top 5 cm for VWC less than 5 kg/m^2. Our retrieved results show the best ubRMSE around 0.05 m^3/m^3, which is close to SMAPs requirement. The observed accuracy of 0.05 m^3/m^3 should be sufficient for landslides. Additional work is needed to better understand the soil-moisture accuracy requirements for landslides that respond to changes in soil moisture of different spatial and temporal scales. However, given the smallest size of slow-moving landslides in the Eel River area is ∼50 × 100 m [9], we find that a spatial scale of 20 m should be sufficient to resolve soil-moisture variations within these landslides. We further note that improved temporal resolution at weekly to monthly timescales would help better constrain the changes in soil moisture that drive these landslides.

E. Sensitivity Test for Soil-Moisture Retrieval

We tested the sensitivity of the model by performing tests against local incidence angle variation and grass stalk orientation.

1) Sensitivity Test to the Local Incidence Angle: The local incidence angle for the UAVSAR data is derived from the look vector of UAVSAR radar and the topography from the SRTM DEM. The SRTM DEM has a coarse pixel resolution of ∼30-m, while the multilooked UAVSAR backscattering has a 6-m pixel resolution. Within a 6 × 6 m range at Two Towers, the slope angle ranged from 4° to 15° according to 1-m pixel resolution airborne lidar [54], while the angle from SRTM was 15°. To assess the impact of the coarse SRTM DEM on the backscattering model simulation, we explored values between 30° and 50° to see how much the model responds (see Table IV). At lower incidence angles (i.e., 30°), there is a stronger contribution from surface

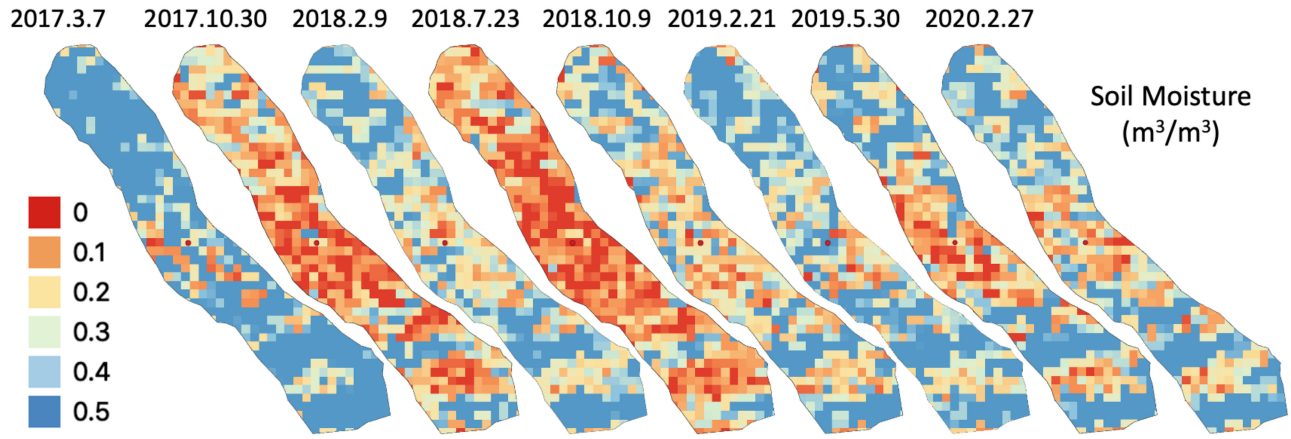

Fig. 11. Time series retrieved soil-moisture map for the Two Towers landslide. Ground-based monitoring location is shown by the red dot. (Retrieval is performed twice using *HH* and *VV*; pixel size: 6 × 6 m).

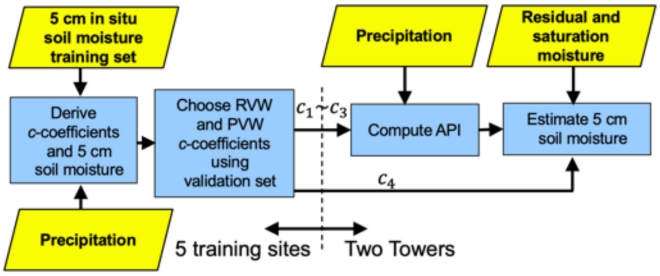

Fig. 12. Flowchart of 5-cm soil-moisture estimation at Two Towers.

TABLE V
SENSITIVITY TO LOCAL INCIDENCE ANGLE UBRMSE AND RMSE (WITHIN PARENTHESES) OF SOIL-MOISTURE RETRIEVAL IN M^3/M^3 USING *HH* AND *VV*, *VV*-ONLY, AND *HH*-ONLY INPUTS

Polarization	30°	44°	50°
HH&VV	0.048 (0.050)	0.055 (0.066)	0.060 (0.068)
VV-only	0.066 (0.066)	0.108 (0.112)	0.112 (0.117)
HH-only	0.060 (0.062)	0.054 (0.054)	0.053 (0.053)

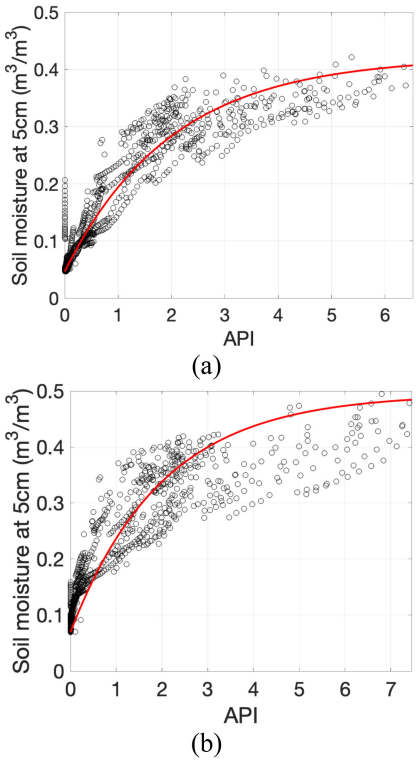

Fig. 13. Soil moisture at 5 cm versus antecedent precipitation index (API) for both *in situ* data and best-fitting curve (red line). (a) NOAA RVW. (b) NOAA PVW.

scattering established by scattering physics. Surface scattering boosts the total backscattering to be closer to the measurement and improves the RMSE for both polarizations. At larger incidence angles (e.g., 50°), backscattering is underestimated due to the reduced contribution from surface scattering, which causes a reduction in correlation and ubRMSE.

For the retrieval, Table V presents that the performance is robust with a similar accuracy within 30° and 50° if we use *HH* and *VV* or *HH*-only to retrieve soil moisture. The retrieval performance at larger incidence angles deteriorated when using *VV*-only. *VV* is dominated by volume scattering, which causes *VV* to become less responsive to soil-moisture changes. Although the surface scattering is minimized at larger angles for *HH*-only retrievals as well as in *VV*, there is still a significant component of double bounce, which provides the sensitivity of backscattering to soil moisture. For the retrieval using *HH* and *VV*, it mitigates the aforementioned weakness in *VV* at a higher incidence angle and stabilizes the retrieval by exploiting the described merit in *HH*. In summary, although from 30° to 50°, RMSE for forward model comparison can vary up to 1–2 dB, while the RMSE for retrieved soil moisture is stable using *HH* and *VV*. This result demonstrates that the retrieval has the tolerance for the topography error while preserving the accuracy.

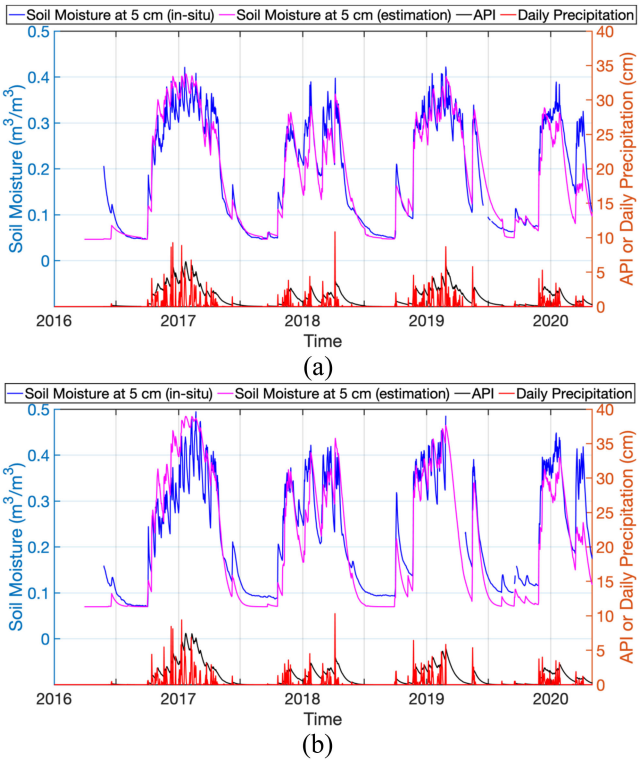

Fig. 14. Time-series soil moisture at 5 cm comparison between the *in situ* measurement and estimated values. (a) NOAA RVW. (b) NOAA PVW.

TABLE VI
SENSITIVITY TO GRASS CYLINDER ANGLE DISTRIBUTION: 0°–66° VERSUS 0°–90° (IN PARENTHESES) OF SOIL-MOISTURE RETRIEVAL IN m^3/m^3

Polarization	RMSE (m^3/m^3)	CORR	ubRMSE (m^3/m^3)
HH&VV	0.066 (0.081)	0.89 (0.84)	0.055 (0.071)
VV-only	0.112 (0.081)	0.73 (0.84)	0.108 (0.074)
HH-only	0.054 (0.101)	0.88 (0.70)	0.055 (0.085)

2) Sensitivity Test to Orientation of the Grass Stalk: The orientation distribution of the grass stalk is an important input in modeling backscattering. Currently, we use a uniform distribution between 0° and 66° for grass cylinders. This range was based on the field observation that grass stalks had a wide range of orientations. To test the sensitivity of our soil-moisture retrieval to orientation, we also used a 0°–90° distribution (see Table VI). We found that the retrieval is sensitive to the grass orientation, particularly for *VV*-only or *HH*-only retrieval. For *HH*-only, the RMSE increased for the 0°–90° orientation. However, we found a decrease in RMSE when using *HH* and *VV* for the retrieval. The change in RMSE is 0.015 m^3/m^3, and the correlation difference is 0.05 for the two different orientation distributions. Therefore, similar to the sensitivity test for the local incidence angle, using both *HH* and *VV* data provides the best performance for soil-moisture retrieval.

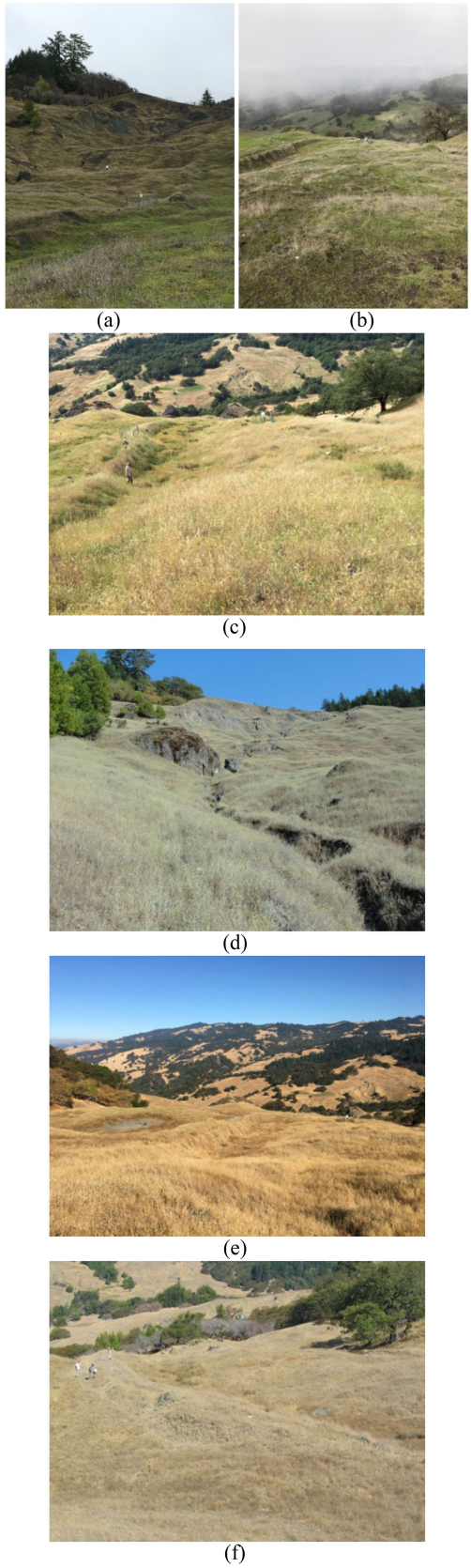

Fig. 15. Field photographs of the Two Towers station (W. Schulz, public domain). (a) January 19, 2013. (b) February 23, 2017. (c) June 14, 2016. (d) July 24, 2013. (e) August 30, 2013. (f) September 29, 2012.

V. Conclusion

This article is aimed at providing a reliable method for estimating the near-surface soil moisture at active landslide zones. The high-resolution soil-moisture maps are necessary to help quantify the hydrological controls on the landslide motion. The key accomplishments of this article are as follows.

1) We apply a physically based model of the grasslands in mountainous terrain where landslides frequently occur. We used backscattering data from NASA's UAVSAR to retrieve soil moisture at 6-m resolution along a 15° hillslope on an active landslide. The ubRMSE from the progressive time-series retrieval process is about 0.06 m^3/m^3 with the correlation of 0.89 using the *HH* and *VV* polarizations.
2) The inversion of the physically based model was successfully applied to two locations with different conditions of slope and vegetation of the same grass landcover, as verified over California and Canada (see Section IV-D).
3) We find that the two copolarized input (*HH* and *VV*) observations provide the most robust soil-moisture retrieval. The two copolarized data are least sensitive to local incidence angle and grass orientation (see Section IV-E), which greatly benefits the applicability of the algorithm in the presence of uncertainties in the knowledge of DEM slope and scatterer orientation.

Overall, this article shows the potential to apply the physical model for mountainous terrain with grass cover. The forward model inversion would be able to cope with variable incidence angles in hilly terrains by rigorously simulating the changes in the dominant scattering mechanism. Our work demonstrates a procedure to estimate high-resolution near-surface soil moisture on steep mountainous slopes, thereby serving as a boundary condition for an advanced hydrological model for landslide applications.

Appendix A

Fig. 12 shows a flowchart that describes our approach for soil-moisture estimation from rainfall data. We use this empirical model approach since we do not have time-series measurements of 5 cm soil moisture from Two Towers. The left-hand side of the dashed line uses the known *in situ* sites with available 5 cm soil moisture and precipitation to constrain the *c*-coefficients [(7)–(9)]. We computed *c*-coefficients from five field sites and eventually selected two sites that are most similar to Two Towers. The selected *c*-coefficients are applied to the right-hand side of the dashed line. $c_1 - c_3$ together with the precipitation data allow us to generate the antecedent precipitation index (API). We can use (7) and API with the bounded soil-moisture values and c_4 to compute the soil moisture at 5-cm depth. In the following, we demonstrate some intermediate results for those two selected sites.

There are four coefficients applied for API-based soil moisture, $c_1 \sim c_4$. They are determined by using training soil moisture and precipitation data from known sites. Fig. 13 shows the fitting curve using (7) together with the scattered *in situ* data. Note that the regression line is for measured 5-cm depth soil moisture against the calculated API. We use these relationships to estimate the 5-cm soil moisture at Two Towers.

We also validated this approach by using *c*-coefficients to calculate the 5-cm soil moisture at RVW and PVW. They are compared with the ground-based measurements (see Fig. 14).

Appendix B

Fig. 15 shows the *in situ* photos of the Two Towers' stations. The annual change of greenness is consistent with the NDVI change in Fig.2.

Acknowledgment

The authors would like to thank USDA-NRCS-National Soil Survey Center for processing and providing the soil clay fraction map over the study area, the UAVSAR flight and data processing teams for their help with acquiring and processing the data, and Planet Labs for providing imagery to A.L.H. Any use of trade, firm, or product names is for descriptive purposes only and does not imply endorsement by the U.S. Government.

References

[1] M. J. Froude and D. N. Petley, "Global fatal landslide occurrence from 2004 to 2016," *Natural Hazards Earth Syst. Sci.*, vol. 18, no. 8, pp. 2161–2181, 2018.
[2] D. Kirschbaum, T. Stanley, and Y. Zhou, "Spatial and temporal analysis of a global landslide catalog," *Geomorphology*, vol. 249, pp. 4–15, 2015.
[3] R. M. Iverson, "Landslide triggering by rain infiltration," *Water Resour. Res.*, vol. 36, no. 7, pp. 1897–1910, 2000.
[4] M. Berti and A. Simoni, "Field evidence of pore pressure diffusion in clayey soils prone to landsliding," *J. Geophys. Res., Earth Surf.*, vol. 115, no. F3, 2010, Art. no. F03031.
[5] K. Terzaghi, "Mechanism of landslides," in *Application of Geology to Engineering Practice*. Boulder, CO, USA: Geol. Soc. Amer., 1950, pp. 83–123.
[6] S. L. Gariano and F. Guzzetti, "Landslides in a changing climate," *Earth-Sci. Rev.*, vol. 162, pp. 227–252, 2016.
[7] P. Lacroix, A. L. Handwerger, and G. Bièvre, "Life and death of slow-moving landslides," *Nature Rev. Earth Environ.*, vol. 1, pp. 404–419, 2020.
[8] G. L. Bennett, J. J. Roering, B. H. Mackey, A. L. Handwerger, D. A. Schmidt, and B. P. Guillod, "Historic drought puts the brakes on earthflows in northern California," *Geophys. Res. Lett.*, vol. 43, no. 11, pp. 5725–5731, 2016.
[9] A. L. Handwerger, E. J. Fielding, M.-H. Huang, G. L. Bennett, C. Liang, and W. H. Schulz, "Widespread initiation, reactivation, and acceleration of landslides in the northern California coast ranges due to extreme rainfall," *J. Geophys. Res., Earth Surf.*, vol. 124, no. 7, pp. 1782–1797, 2019.
[10] E. H. Rutter and S. Green, "Quantifying creep behaviour of clay-bearing rocks below the critical stress state for rapid failure: Mam tor landslide, Derbyshire, England," *J. Geol. Soc.*, vol. 168, no. 2, pp. 359–372, 2011.
[11] W. H. Schulz, J. B. Smith, G. Wang, Y. Jiang, and J. J. Roering, "Clayey landslide initiation and acceleration strongly modulated by soil swelling," *Geophys. Res. Lett.*, vol. 45, no. 4, pp. 1888–1896, 2018.
[12] J. A. Coe *et al.*, "Seasonal movement of the Slumgullion landslide determined from global positioning system surveys and field instrumentation, July 1998–March 2002," *Eng. Geol.*, vol. 68, no. 1/2, pp. 67–101, 2003.
[13] J.-P. Malet, O. Maquaire, and E. Calais, "The use of global positioning system techniques for the continuous monitoring of landslides: Application to the Super-Sauze earthflow (Alpes-de-Haute-Provence, France)," *Geomorphology*, vol. 43, no. 1/2, pp. 33–54, 2002.
[14] S.-B. Kim, M. Moghaddam, L. Tsang, M. Burgin, X. Xu, and E. G. Njoku, "Models of L-band radar backscattering coefficients over global terrain for soil moisture retrieval," *IEEE Trans. Geosci. Remote Sens.*, vol. 52, no. 2, pp. 1381–1396, Feb. 2014.

[15] B. G. Delbridge, R. Bürgmann, E. Fielding, S. Hensley, and W. H. Schulz, "Three-dimensional surface deformation derived from airborne interferometric UAVSAR: Application to the Slumgullion landslide," *J. Geophys. Res., Solid Earth*, vol. 121, no. 5, pp. 3951–3977, 2016.

[16] A. Stumpf, J.-P. Malet, and C. Delacourt, "Correlation of satellite image time-series for the detection and monitoring of slow-moving landslides," *Remote Sens. Environ.*, vol. 189, pp. 40–55, 2017.

[17] O. Merlin, C. Rudiger, A. Al Bitar, P. Richaume, J. P. Walker, and Y. H. Kerr, "Disaggregation of SMOS soil moisture in southeastern Australia," *IEEE Trans. Geosci. Remote Sens.*, vol. 50, no. 5, pp. 1556–1571, May 2012.

[18] S. Paloscia, S. Pettinato, E. Santi, C. Notarnicola, L. Pasolli, and A. Reppucci, "Soil moisture mapping using Sentinel-1 images: Algorithm and preliminary validation," *Remote Sens. Environ.*, vol. 134, pp. 234–248, 2013.

[19] M. Foucras, M. Zribi, C. Albergel, N. Baghdadi, J.-C. Calvet, and T. Pellarin, "Estimating 500-m resolution soil moisture using Sentinel-1 and optical data synergy," *Water*, vol. 12, no. 3, 2020, Art. no. 866.

[20] R. H. Lang and J. S. Sighu, "Electromagnetic backscattering from a layer of vegetation: A discrete approach," *IEEE Trans. Geosci. Remote Sens.*, vol. GE-21, no. 1, pp. 62–71, Jan. 1983.

[21] H. Huang *et al.*, "Coherent model of L-band radar scattering by soybean plants: Model development, evaluation, and retrieval," *IEEE J. Sel. Topics Appl. Earth Observ. Remote Sens.*, vol. 9, no. 1, pp. 272–284, Jan. 2016.

[22] L. Tsang *et al.*, "Active and passive vegetated surface models with rough surface boundary conditions from NMM3D," *IEEE J. Sel. Topics Appl. Earth Observ. Remote Sens.*, vol. 6, no. 3, pp. 1698–1709, Jun. 2013.

[23] R. Akbar and M. Moghadda, "A combined active-passive soil moisture estimation algorithm with adaptive regularization in support of SMAP," *IEEE Trans. Geosci. Remote Sens.*, vol. 53, no. 6, pp. 3312–3324, Jun. 2015.

[24] M. Kurum, M. Deshpande, A. T. Joseph, P. E. O'Neill, R. H. Lang, and O. Eroglu, "SCoBi-Veg: A generalized bistatic scattering model of reflectometry from vegetation for signals of opportunity applications," *IEEE Trans. Geosci. Remote Sens.*, vol. 57, no. 2, pp. 1049–1068, Feb. 2019.

[25] T. Jagdhuber, I. Hajnsek, and K. P. Papathanassiou, "An iterative generalized hybrid decomposition for soil moisture retrieval under vegetation cover using fully polarimetric SAR," *IEEE J. Sel. Topics Appl. Earth Observ. Remote Sens.*, vol. 8, no. 8, pp. 3911–3922, Aug. 2015.

[26] L. Tsang, J. A. Kong, and K.-H. Ding, *Scattering of Electromagnetic Waves: Theories and Applications,* vol. 1. New York, NY, USA: Wiley, 2000.

[27] T.-H. Liao, S.-B. Kim, S. Tan, L. Tsang, C. Su, and T. J. Jackson, "Multiple scattering effects with cyclical correction in active remote sensing of vegetated surface using vector radiative transfer theory," *IEEE J. Sel. Topics Appl. Earth Observ. Remote Sens.*, vol. 9, no. 4, pp. 1414–1429, Apr. 2016.

[28] S.-B. Kim, L. Tsang, J. T. Johnson, S. Huang, J. J. van Zyl, and E. G. Njoku, "Soil moisture retrieval using time-series radar observations over bare surfaces," *IEEE Trans. Geosci. Remote Sens.*, vol. 50, no. 5, pp. 1853–1863, May 2012.

[29] B. Bauer-Marschallinger *et al.*, "Toward global soil moisture monitoring with Sentinel-1: Harnessing assets and overcoming obstacles," *IEEE Trans. Geosci. Remote Sens.*, vol. 57, no. 1, pp. 520–539, Jan. 2019.

[30] J. D. Ouellette *et al.*, "A time-series approach to estimating soil moisture from vegetated surfaces using L-band radar backscatter," *IEEE Trans. Geosci. Remote Sens.*, vol. 55, no. 6, pp. 3186–3193, Jun. 2017.

[31] W. H. Schulz *et al.*, "Data from in-situ landslide monitoring, Trinity county, California," U.S. Geol. Survey, Reston, VA, USA, 2018. [Online]. Available: https://doi.org/10.5066/F7GF0SFS

[32] W. H. Schulz and J. B. Smith, "Precipitation and soil-moisture data from the two towers landslide, Trinity county, California," U.S. Geol. Survey, Reston, VA, USA, 2020. [Online]. Available: https://doi.org/10.5066/P9NSUMOY

[33] PRISM Climate Group, Oregon State Univ., Feb. 2004. [Online]. Available: http://prism.oregonstate.edu

[34] Google. [Google Maps, the Two Towers]. Accessed: Sep./Oct. 2020. [Online]. Available: https://goo.gl/maps/WP7pQE2KJXh4yPVz8

[35] C. G. Homer, J. A. Fry, and C. Barnes, "The National Land Cover Database," U.S. Geol. Survey, Reston, VA, USA, 2012.

[36] N. Bliss, J. Thompson, J. Hempel, and Z. Libohova, GlobalSoilMap version 0.5: Soil property maps from the state soil geography (SSURGO) database filled in with general soil map database (STATSG02) database for the lower 48 states, 2017.

[37] A. S. Jayko, M. C. Blake, R. J. McLaughlin, H. N. Ohlin, S. D. Ellen, and H. M. Kelsey, "Reconnaissance geologic map of the Covelo 30- by 60-minute Quadrangle, Northern California (No. MF-2001)," United States Geol. Survey, Reston, VA, USA, 1989. [Online]. Available: http://ngmdb.usgs.gov/Prodesc/proddesc_327.htm

[38] R. J. McLaughlin *et al.*, Geologic map of the Cape Mendocino, Eureka, Garberville, and Southwestern part of the Hayfork 30 X 60 Quadrangles and adjacent offshore area, Northern California, CA, USA, 2000.

[39] W. J. Hahm *et al.*, "Lithologically controlled subsurface critical zone thickness and water storage capacity determine regional plant community composition," *Water Resour. Res.*, vol. 55, no. 4, pp. 3028–3055, 2019.

[40] D. N. Dralle, W. J. Hahm, D. M. Rempe, N. J. Karst, S. E. Thompson, and W. E. Dietrich, "Quantification of the seasonal hillslope water storage that does not drive streamflow," *Hydrol. Processes*, vol. 32, no. 13, pp. 1978–1992, 2018.

[41] R. M. Iverson and J. J. Major, "Rainfall, ground-water flow, and seasonal movement at minor creek landslide, northwestern California: Physical interpretation of empirical relations," *Geol. Soc. Amer. Bull.*, vol. 99, no. 4, pp. 579–594, 1987.

[42] A. L. Nereson, S. D. Olivera, and N. J. Finnegan, "Field and remote-sensing evidence for hydro-mechanical isolation of a long-lived earthflow in central California," *Geophys. Res. Lett.*, vol. 45, no. 18, pp. 9672–9680, 2018.

[43] C. J. Tucker, "Red and photographic infrared linear combinations for monitoring vegetation," *Remote Sens. Environ.,* vol. 8, no. 2, pp. 127–150, 1979.

[44] K. Didan, "MOD13Q1 MODIS/terra vegetation indices 16-Day L3 global 250m SIN grid V006," NASA EOSDIS LP DAAC, Sioux Falls, SD, USA, 2015.

[45] S. Huang and L. Tsang, "Electromagnetic scattering of randomly rough soil surfaces based on numerical solutions of Maxwell equations in three-dimensional simulations using a hybrid UV/PBTG/SMCG method," *IEEE Trans. Geosci. Remote Sens.*, vol. 50, no. 10, pp. 4025–4035, Oct. 2012.

[46] Y. Oh and Y. C. Kay, "Condition for precise measurement of soil surface roughness," *IEEE Trans. Geosci. Remote Sens.*, vol. 36, no. 2, pp. 691–695, Mar. 1998.

[47] Y. Gao, J. P. Walker, M. Allahmoradi, A. Monerris, D. Ryu, and T. J. Jackson, "Optical sensing of vegetation water content: A synthesis study," *IEEE J. Sel. Topics Appl. Earth Observ. Remote Sens.*, vol. 8, no. 4, pp. 1456–1464, Apr. 2015.

[48] E. R. Hunt, L. Li, M. T. Yilmaz, and T. J. Jackson, "Comparison of vegetation water contents derived from shortwave-infrared and passive-microwave sensors over central Iowa," *Remote Sens. Environ.*, vol. 115, no. 9, pp. 2376–2383, 2011.

[49] M. H. Cosh, J. Tao, T. J. Jackson, L. McKee, and P. E. O'Neill, "Vegetation water content mapping in a diverse agricultural landscape: National airborne field experiment 2006," *J. Appl. Remote Sens.*, vol. 4, no. 1, 2010, Art. no. 043532.

[50] E. Vermote, C. Justice, M. Claverie, and B. Franch, "Preliminary analysis of the performance of the Landsat 8/OLI land surface reflectance product," *Remote Sens. Environ.*, vol. 185, pp. 46–56, 2016.

[51] P. Team, Planet application program interface, in *Space for Life on Earth.* San Francisco, CA, USA, 2017. [Online]. Available: https://api.planet.com

[52] F. Pan, "Estimating daily surface soil moisture using a daily diagnostic soil moisture equation," *J. Irrigation Drainage Eng.*, vol. 138, no. 7, pp. 625–631, 2012.

[53] F. Pan, C. D. Peters-Lidard, and M. J. Sale, "An analytical method for predicting surface soil moisture from rainfall observations," *Water Resour. Res.*, vol. 39, no. 11, 2003, Art. no. 1314.

[54] J. J. Roering, Eel River, CA: Landsliding and the Evolution of Mountainous Landscapes, National Center for Airborne Laser Mapping, 2012. [Online]. Available: https://doi.org/10.5069/G9XS5S9P

[55] H. McNairn *et al.*, "The soil moisture active passive validation experiment 2012 (SMAPVEX12): Prelaunch calibration and validation of the SMAP soil moisture algorithms," *IEEE Trans. Geosci. Remote Sens.*, vol. 53, no. 5, pp. 2784–2801, May 2015.

[56] V. L. Mironov, M. C. Dobson, V. H. Kaupp, S. A. Komarov, and V. N. Kleshchenko, "Generalized refractive mixing dielectric model for moist soils," *IEEE Trans. Geosci. Remote Sens.,* vol. 42, no. 4, pp. 773–785, Apr. 2004.

[57] L. Pasolli *et al.*, Estimation of soil moisture in mountain areas using SVR technique applied to multiscale active radar images at C-band, *IEEE J. Sel. Topics Appl. Earth Observ. Remote Sens.*, vol. 8, no. 1, pp. 262–283, Jan. 2015.

Tien-Hao Liao received the B.S. degree in mathematics from National Taiwan University, Taipei, Taiwan, in 2003, M.S. degree in communication engineering from National Chiao Tung University, Hsinchu, Taiwan, in 2005, and the Ph.D. degree in electrical engineering from the University of Washington, Seattle, USA, in 2015.

He was a Research Fellow with the Radiation Laboratory, University of Michigan. His research interest focuses on the electromagnetic scattering model for the natural terrain, waveguides, and the topological photonics. For microwave remote sensing over the vegetated and rough surface, his research was applied for the soil moisture retrieval in the NASA SMAP mission. He also applies L-band interferometry to study the wetlands to demonstrate the capability of the coming NISAR mission. Dr. Liao was a recipient of the NASA Postdoctoral Program fellowship to do the research with Jet Propulsion Laboratory.

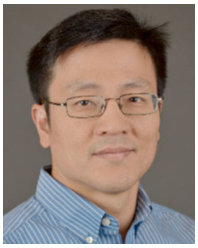

Seung-Bum Kim received the B.S. degree in electrical engineering from the Korea Advanced Institute of Science and Technology (KAIST), in 1992 and the M.S. and Ph.D. degrees in remote sensing from the University College London, England, in 1993 and 1998, respectively.

Since 2009, he has been a Scientist with Remote Sensing Systems, California, studying the L-band radiometry for the Aquarius salinity observation with the Jet Propulsion Lab. The current research includes microwave modeling and soil moisture retrieval with the radar.

Dr. Kim has been a member of the Aquarius, SMAP, and NISAR science teams.

Alexander L. Handwerger received the B.A. degree in earth sciences from Boston University, Boston, MA, USA, in 2008, and the Ph.D. degree in geological sciences from the University of Oregon, Eugene, OR, USA, in 2015.

He is currently an Assistant Researcher at the Joint Institute for Regional Earth System Science and Engineering (JIFRESSE), University of California, Los Angeles (UCLA), CA, USA. JIFRESSE is a scientific collaboration between UCLA and the Jet Propulsion Laboratory, California Institute of Technology, to improve understanding and to develop future projections about global climate change and its effect on regional climates and environments. His research interests include landslides, rock glaciers, and satellite and airborne interferometric synthetic aperture radar.

Eric J. Fielding received the B.A. degree in earth sciences from Dartmouth College, Hanover, NH, USA in 1982, and the Ph.D. degree in geological sciences from Cornell University, Ithaca, NY, USA in 1989.

Since 1994, he has been a Research Scientist with Jet Propulsion Laboratory, California Institute of Technology, Pasadena, CA, USA. He was also a Research Scientist with the University of Oxford, Oxford, U.K., and a Visiting Research Scientist with he University of Cambridge, Cambridge, U.K. His current research interests include the application of synthetic aperture radar interferometry to measuring deformation on and around faults before, during, and after earthquakes and on landslides.

Dr. Fielding was a recipient of the Ivan I. Mueller Award from the AGU Geodesy section and two NASA Exceptional Scientific Achievement medals. He is a member of the American Geophysical Union, the Geological Society of America, and the Seismological Society of America.

Michael H. Cosh (Senior Member, IEEE) received the Ph.D. degree in civil and environmental engineering from Cornell University, Ithaca, NY, USA, in 2002.

He is a Research Hydrologist with the U.S. Department of Agriculture, Agricultural Research Service, Hydrology and Remote Sensing Laboratory, Beltsville, MD, USA. His current research interests include the monitoring of soil moisture from both *in situ* resources and satellite products. He conducts research on satellite calibration and validation for such missions as the soil moisture active passive and soil moisture ocean salinity missions.

Dr. Cosh is a fellow of the American Society of Agronomy.

William H. Schulz received the B.S. degree in geology from the University of Wisconsin-Milwaukee, Milwaukee, WI, USA, in 1994, the M.S. degree in engineering geology from Purdue University, West Lafayette, IN, USA, in 1996, and the Ph.D. in engineering geology from Kyoto University, Kyoto, Japan, in 2020.

Since 2002, he has been employed as a Research Geologist with the Landslide Hazards Program of the U.S. Geological Survey. His research focuses on improving the understanding of mechanisms controlling landslide reactivation and motion under variable forcing.